ACS APPLIED MATERIALS & INTERFACES

Article

Multi-material 3D printing of Graphene-based electrodes for Electrochemical Energy Storage using Thermo-Responsive Inks

Victoria García Rocha, Esther Garcia-Tunon, Cristina Botas, Foivos Markoulidis, Ezra Feilden, Eleonora D'Elia, Na Ni, Milo Sebastian Peter Shaffer, and Eduardo Saiz

ACS Appl. Mater. Interfaces, **Just Accepted Manuscript** • DOI: 10.1021/acsami.7b10285 • Publication Date (Web): 18 Sep 2017

ACS Publications

ACS Applied Materials & Interfaces is published by the American Chemical Society. 1155 Sixteenth Street N.W., Washington, DC 20036

Multi-material 3D printing of Graphene-based electrodes for Electrochemical Energy Storage using Thermo-Responsive Inks

Journal:	*ACS Applied Materials & Interfaces*
Manuscript ID	am-2017-102853.R2
Manuscript Type:	Article
Date Submitted by the Author:	n/a
Complete List of Authors:	Rocha, Victoria; Cardiff University Cardiff School of Engineering, School of Engineering Garcia-Tunon, Esther; University of Liverpool, Materials Innovation Factory and School of Engineering Botas, Cristina; CIC Energigune, Markoulidis, Foivos; Imperial College London, Department of Chemistry Feilden, Ezra ; Imperial College London, Department of Materials D'Elia, Eleonora; Imperial College London, Department of Materials Ni, Na; Imperial College London, Shaffer, Milo; London Imperial College, Department of Chemistry Saiz, Eduardo; Imperial College, Material Science

Multi-material 3D printing of Graphene-based electrodes for Electrochemical Energy Storage using Thermo-Responsive Inks

Victoria G. Rocha[1,2], Esther García-Tuñón*[1,3], Cristina Botas[4] ,Foivos Markoulidis[1,5], Ezra Feilden[1], Eleonora D'Elia[1], Na Ni[1], Milo Shaffer[1,5] and Eduardo Saiz[1]*

[1]Department of Materials, Centre for Advanced Structural Ceramics, Imperial College London, London SW7 2AZ, UK

[2]School of Engineering, Cardiff University, Cardiff, CF24 3AA, UK

[3]School of Engineering & Materials Innovation Factory, University of Liverpool, Liverpool, L69 3GH, UK

[4]CIC Energigune, Parque Tecnológico de Álava, Albert Einstein 48, 01510 Miñano, Álava, Spain

[5]Department of Chemistry, Nanostructured Hierarchical Assemblies and Composites Group, Imperial College London, London SW7 2AZ, UK

E-mail: GarciaRochaV@cardiff.ac.uk, Esther.GTunon@liverpool.ac.uk

Abstract

The current lifestyles, increasing population and limited resources result in energy research being at the forefront of worldwide grand challenges, increasing the demand for sustainable and more efficient energy devices. In this context, Additive Manufacturing brings the possibility of making electrodes and electrical energy storage (EES) devices in any desired 3D shape and dimensions, while preserving the multifunctional properties of the active materials in terms of surface area and conductivity. This paves the way to optimized and more efficient designs for energy devices. Here we describe how three-dimensional (3D) printing will allow the fabrication of bespoke devices - with complex geometries, tailored to fit specific requirements and applications - by designing water-based thermo-responsive inks to 3D-print different materials in one step. For example, printing the active material precursor (Chemically Modified Graphene, rCMG) and the current collector (copper) for supercapacitors or anodes for Lithium-ion batteries (LIBs). The formulation of thermo responsive inks using Pluronic F127 provides an aqueous-based, robust, flexible and easy scalable-up approach. The devices are designed to provide low resistance interface, enhanced electrical properties, mechanical performance, packing of rCMG and low active material density while facilitating the post-processing of the multicomponent 3D printed structures. The electrode materials are selected to match post-processing conditions. The reduction of the active material (rCMG) and sintering of the current collector (Cu) take place simultaneously. The electrochemical performance of the rCMG-based self-standing binder-free electrode and the two-materials rCMG/Cu printed prove the potential of multi-material printing in energy applications.

Keywords: graphene oxide, graphene-based devices, colloidal processing, additive manufacturing, 3D printing.

Introduction

Additive manufacturing (AM) technologies, based on making a 3D object of virtually any shape from a digital model, open up completely new possibilities to design and fabricate devices and structures. AM promises integrated, customized and unusually shaped components with improved performance that can be created on demand in a one-step process. On the other hand, graphene with its unique intrinsic properties, is expected to revolutionize a wide range of applications including membranes[1], multifunctional composites[2], Joule Heaters,[3] supercapacitors,[4] Li-ion Batteties (LIBs)[5], redox-flow batteries[6], among other energy applications[7]. The integration of graphene in AM is attracting increasing attention as a path to extend its practical applications[8-9]. This is particularly attractive in the context of electrodes and devices for EES[10-13]. Despite the continuous progress on graphene research and AM, there are still many issues to address, for example combining graphene with other materials or retaining its unique intrinsic properties during the process.[14] Graphene, with a theoretical surface area of 2600 $m^2 g^{-1}$, high electrical conductivity and mechanical robustness has the potential to improve the performance of EES current devices. The current routes to prepare an electrode for an EES system show two main limitations. First, they require a significant amount of binder (>5 wt%) to prepare slurries or inks that can be used to coat current-collecting foils which are then laminated into thin films and integrated into pouch, prismatic or button cells. Their performance is hindered as the binder increases the electrical resistivity of the electrode. Conductive additives such as carbon black or carbon nanotubes (CNTs)[15] are often used to mitigate these problems. A

promising approach involves the preparation of aerogels based on binder-free graphene[16,17-18] or CNTs [19,20] as 3D seamless electrodes.

A huge effort is currently being made on the wet processing of aerogels and 3D structures from graphene-related 2D materials.[21,22] Secondly, they show limited performance due to the thin-film configuration which provides insufficient interfacial areas for energy storage. Recent research provides different alternatives to integrate 2D materials into direct ink writing (DIW) as an efficient way to increase the areal drawback.[17,23-24] This AM technique enables 3D printing of any material that can be processed into a paste with optimised viscoelastic flow; it also allows building multi-material 3D structures with fine resolution while minimizing waste[25]. One of the first EES devices using DIW consisted of an interdigitated micro-battery.[26] More recently a full cell combining electrodes of Graphene Oxide and Lithium iron phosphate ($LiFePO_4$, LFP) and lithium titanium oxide ($Li_4Ti_5O_{12}$, LTO) as cathode and anode materials was also made using DIW.[27] Both studies are example of the potential of DIW in energy devices but despite the rapid progress in the field there are still fundamental challenges to overcome. It is necessary to provide more flexible, robust and simple water-based approaches for multi-material printing, avoiding complicated bespoke formulations and solvent based systems.

In this work we address the challenge of assembling 2D colloids of CMG with other materials to build multi-material devices using an AM technique based on the continuous extrusion of colloidal inks at room temperature. This process enables the direct printing of electrodes for EES in any desired 3D shape and dimensions, while preserving the multifunctional properties of the active materials in terms of surface area and conductivity. The challenge is to formulate colloidal inks of different materials with matching flow behavior and viscoelasticity to manufacture multi-component electrodes for EES applications. Here, we use an aqueous-based thermo-responsive

formulation to fabricate proof-of-concept electrodes combining chemically modified graphene (CMG) as active material and copper as current collector. Copper, a common current collector of anodes for LIBs, is selected as archetypical example of a high-conductivity metallic track whose sintering conditions match the thermal treatment required to reduce the CMG aerogels in the electrode. These formulations are water-based, non-toxic, flexible and easily scalable up, facilitating the design of inks containing different materials (in terms of shape, size, chemistry and surface area) from 2D materials (CMG) to metallic particles (Cu) with optimized rheological behavior to 3D print multi-material devices.

Experimental Methods

Materials. Spherical copper powder was purchased from Alfa Aesar with average particle size of 10 micron and purity of 99.9% (metals basis). Tens of grams of Chemically Modified Graphene (CMG) were reproducibly and safely prepared using a modified procedure from Tour et al.,[28] using natural graphite powder, Aldrich. (Supporting Information). Pluronic® F-127 powder, BioReagent, suitable for cell culture was purchased from Sigma Aldrich. Supercapacitor components: cellulose paper separator (TF4060, Nippon Kodoshi Corp.), "nanowhisker" Al foil tab (Toyal Carbo®, Toyo Aluminiurn K.K.) and 1-ethyl-3-methylimidazolium bis(trifluoromethylsulfonyl)imide (EMI-TFSI, 99%, Iolitec) electrolyte.

CMG synthesis was performed in a custom-built reactor designed to manipulate up to 10 L of concentrated acids. In a typical synthesis, a 9:1 mixture of concentrated H_2SO_4/H_3PO_4 (3:0.3 L) was mixed with 24 g of natural graphite flakes (150-500 μm sieved, Aldrich), followed by the addition of 144 g of $KMnO_4$ (6 wt%). This slightly exothermic reaction increased the temperature up to 35-40 °C during the mixing process. Afterwards, the temperature controller was set at 50 °C while stirring vigorously at 400 rpm for 18 h. Once completed, the reactor was

cooled down to room temperature and a peristaltic pump was used for the slow addition of 1.72 L of aqueous H_2O_2 (2 wt%) that stopped the oxidation. The graphene oxide suspension was washed using repeated centrifugation at 9000 rpm (Thermo Scientific Sorvall LYNX 6000 super speed Centrifuge) and re-dispersion in double-distilled water. The work-up was carried out until the supernatant water of the centrifuged CMG was close to pH 6, typically occurring after 16 washing cycles. Low speed (<1000 rpm) centrifugation cycles were performed to remove any un-exfoliated graphite particles.

CMG characterization. The lateral dimensions of the CMG flakes were measured using optical microscopy (Axio Scope A1, Zeiss). The CMG content in the slurry was estimated from freeze-dried CMG samples. Thermogravimetric analysis (TG 449 F1 Jupiter Thermo-Nanobalance, NETZSCH) was performed to evaluate the presence of impurities by heating the freeze-dried GO up to 800 °C at 10 °C min^{-1} in air. Carbon content was verified by elemental analysis.

Pluronic stock solution preparation. A Thinky ARE-250 Mixer was used to prepare a Pluronic® F-127 stock solution (25 wt%) that was stored in a fridge for 24 h to facilitate the mixing (below the transition temperature (~17 °C) for F127 solution where its viscosity is very low). Until the stock solution became transparent a consecutive sequence of steps of 2 minutes mixing, 2 minutes de-foaming and 15 minutes cooling (below LCST) are followed to obtain a homogeneous solution that is then ready to prepare the inks.

Ink formulation. A 25wt% Pluronic® F-127 aqueous stock solution was prepared using a Thinky ARE-250 Mixer in a sealed HDPE thick wall container. The copper ink was prepared using the F-127 stock solution and copper powder with solid loading up to 85 wt% to achieve the desired rheological behavior. CMG inks have been prepared from freeze dried CMG with a fixed weight ratio CMG:Pluronic® F-127 of 1:1. Cu powders and CMG flakes were mixed with F127

solutions in an ice bath prior homogenization and defoaming with Thinky ARE-250. The final solids content of the CMG inks varied between 2.5 and 6 wt%. Cu inks were prepared by mixing 10 μm spherical Cu particles (up to 85 wt%) with a 25 wt% aqueous F127 stock solution. The inks were prepared at least 24h beforehand to ensure stable rheological response.

Ink rheology. The flow behaviour and viscoelastic properties of the copper and CMG inks were measured in a Discovery Hybrid Rheometer HR1 (TA Instruments) with a parallel plate (ø = 40 mm) and a solvent trap cover. The viscoelastic properties (G', G'') were assessed with strain and frequency sweeps, and the effect of the temperature was monitored with a temperature ramp. In detail, viscoelastic fingerprints and linear viscosity region (LVR) were evaluated with stress-controlled amplitude sweeps at a fixed frequency of 396 rad/s, and stress-controlled frequency sweeps at a fixed strain of 0.15%.

Printing. Copper and CMG inks were used to print a 3D object in a single step using a robotic deposition device (Robocad 3.0, 3-D inks Stillwater, OK) on a 0.5 mm thickness graphite paper.

Post-processing. The printed electrodes were frozen in liquid nitrogen and freeze dried for 48 h (Freezone 4.5, Labconco Corporation) followed by thermal reduction at 900 ^{o}C for 1h under 10%H_2/90%Ar atmosphere.

Structural, mechanical and electrochemical characterization. Printed samples and devices were thoroughly characterised using BET, FESEM, Raman spectroscopy, XPS, TEM and TGA as well as compression tests while monitoring their electrical conductivity.

Specific surface, BET values were obtained using nitrogen physisorption at 77K in a 3 Flex (Micromeritics, USA). The sample was degassed under vacuum for 16 h at 120 °C followed by in-situ degassing at 120 °C for 4 h. BET surface area calculation was obtained from N2 isotherm using 3Flex Version 3.02 software package (Micromeritics, USA).

CMG and rCMG objects were also characterized by FESEM, XPS and its electrical conductivity by 4-point probe method.

FEGSEM. Structural features were analysed at 5kV with field emission scanning electron microscopy on a LEO Gemini 1525 FEGSEM equipped with an energy dispersive spectroscopy (EDS) microprobe (INCA Sight Oxford-instruments, UK). All samples were coated with a thin Cr layer before the observation.

Transmission electron microscopy (TEM) and Scanning TEM (STEM) of the r-CMG electrode flakes were carried out using a FEI Titan 80-300 S/TEM operated at 80 kV

X-ray photoelectron spectroscopy (XPS). Analyses were performed on dried CMG, 3D-printed CMG:Pluronic and r-CMG 3D printed networks using a K-Alpha spectrometer (ThermoFisher Scientific; East Grinstead, UK). XPS spectra were acquired using a microfocused monochromatic Al Kα X-ray source (hυ = 1486.6 eV). An X-ray spot of ~400x800 μm ellipse shape was used and three different areas were spotted. Core level C1s, C_{KLL}, O1s, N1s, Mn1s, S2p, Na1s spectra were acquired using a pass energy of 200 eV and high regions at 40eV.

XPS Data Analysis. Casa XPS was used for data interpretation. Shirley or two point linear background subtractions were employed depending on background shape. Scofield cross-sections were used as relative sensitivity factors in the calculation of the atomic percentages (with RSF of C 1s = 1.000). Peaks were fitted using GL(30) lineshapes; a combination of a Gaussian (70%) and Lorentzian (30%). All XP spectra were charge corrected by referencing the fitted contribution of C-C graphitic like carbon in the C 1s signal to 284.6 eV. The atomic percentages were calculated from the peak areas in the acquired high resolution C 1s and O 1s photoelectron spectra using Scofield sensitivity factors.

Raman spectra were recorded with a Renishaw Raman inVia microscope using a 532 nm excitation laser source at a laser power of 1.5 mW. The spectra were collected over an area of 25x25 μm^2 and an average spectrum was calculated.

Mechanical characterization. The mechanical tests were carried out in a Zwick universal testing machine with a maximum load of 2 kN. The 3D structures were subjected to cyclic compression in the direction perpendicular to the printing plane: up to 5 cycles at 10% and 20% strain, with a holding period of 30s under position-controlled movement of 1 mm min-1.

Electrical conductivity. A standard 4-point probe method was used for conductivity measurements. The current was generated via a bench top PSU and kept at a constant direct current of 10 mA. Two electrodes were placed through the sample at constant distance to monitor the voltage drop through the sample. The results were derived via standard equations for electrical conductivity and resistivity in DC.

Electrochemical characterization (EIS and CVs) was carried out using a Potentiostat/Galvanostat/ZRA, Gamry Instruments, Inc. Reference 600^{TM}. Data analysis and fitting were completed using the Gamry Framework, EChem Analyst. Electrochemical tests in EMI-TFSI were performed using the following setups, assembled under nitrogen atmosphere: i) 3 electrodes system: rCMG (rectangular grid, dimensions: 5.0 mm, 4.8 mm and 3.4 mm, Figure 1e) was using as working electrode, silver wire as counter electrode and Ag/AgCl (3M NaCl) as reference electrode (Figure S7). ii) Pouch cell: symmetric double-layer capacitor (EDLC) with 3D printed rCMG/Cu-based samples as electrodes and cellulose paper as separator (Figure 3). Further details and protocols can be found in the Supporting Information.

RESULTS AND DISCUSSION

Ink formulation, rheology and printing

The colloidal inks are based on a commercially available thermo responsive polymer (Pluronic F127, BASF). F127 in water forms a hydrogel able to carry any particle system such as ceramics with different compositions and particle shapes.[29,30] F127 is a tri-block non-ionic copolymer (PEO-PPO-PEO) that in solution responds to temperature by changing its configuration and as a consequence its flow and viscoelastic behaviour. At temperatures below lower critical solution temperature (< LCST), all three components in the tri-block are hydrophilic and its viscosity is very low. At temperatures above its LCST, PPO becomes hydrophobic leading to a change in the tri-block conformation, with the formation of micelles, that considerable increase viscosity. These hydrogels are a very versatile and robust carrier to control the flow and viscoelasticity of most materials. Inks with a wide range of solid contents are formulated by mixing CMG (Figure S1, Supporting Information) or Cu powders with F127 water solutions at a temperature of ~4°C (well below the LCST of ~17°C, Figure 1a). At room temperature (>LCST), the CMG flakes and F127 micelles assemble into a network, forming a soft solid with high viscosity and elastic behaviour (Figure 1a-c). The oxygen functionalities distributed in the edges and surface of CMG flakes facilitate multiple F127-CMG interactions leading to an assembled network. We propose the following mechanism: at temperatures below LCST, the PEO components in F127 tri-blocks may establish hydrogen bonds with carboxyl and hydroxyl functional groups in edges and basal planes in CMG. When the temperature rises over the LCST (between 15-19°C for Cu and CMG inks with different solid and F127 concentrations, Figure 1c), the central part in the tri-block (poly(propylene oxide) (PPO)) becomes hydrophobic. This results in the formation of hydrogel micelles and in hydrophobic interactions of the PPO segment with the un-oxidised aromatic

islands on the basal plane of CMG flakes.[31,32] These 3D assemblies result in soft solids with very flexible rheology depending on the CMG content (Figure 1). Inks with concentrations between 2 and 6 wt% prepared from freeze-dried CMG (CMG:F127, 1:1 (dry weight)) display good viscoelastic flow for DIW. 3D structures with very different shapes and sizes (Figure 1d-f) were built following a computer design in a robocaster using nozzles with diameters ranging from 1000 μm down to 100 μm at printing speeds between 6 and 12 mm s^{-1}.

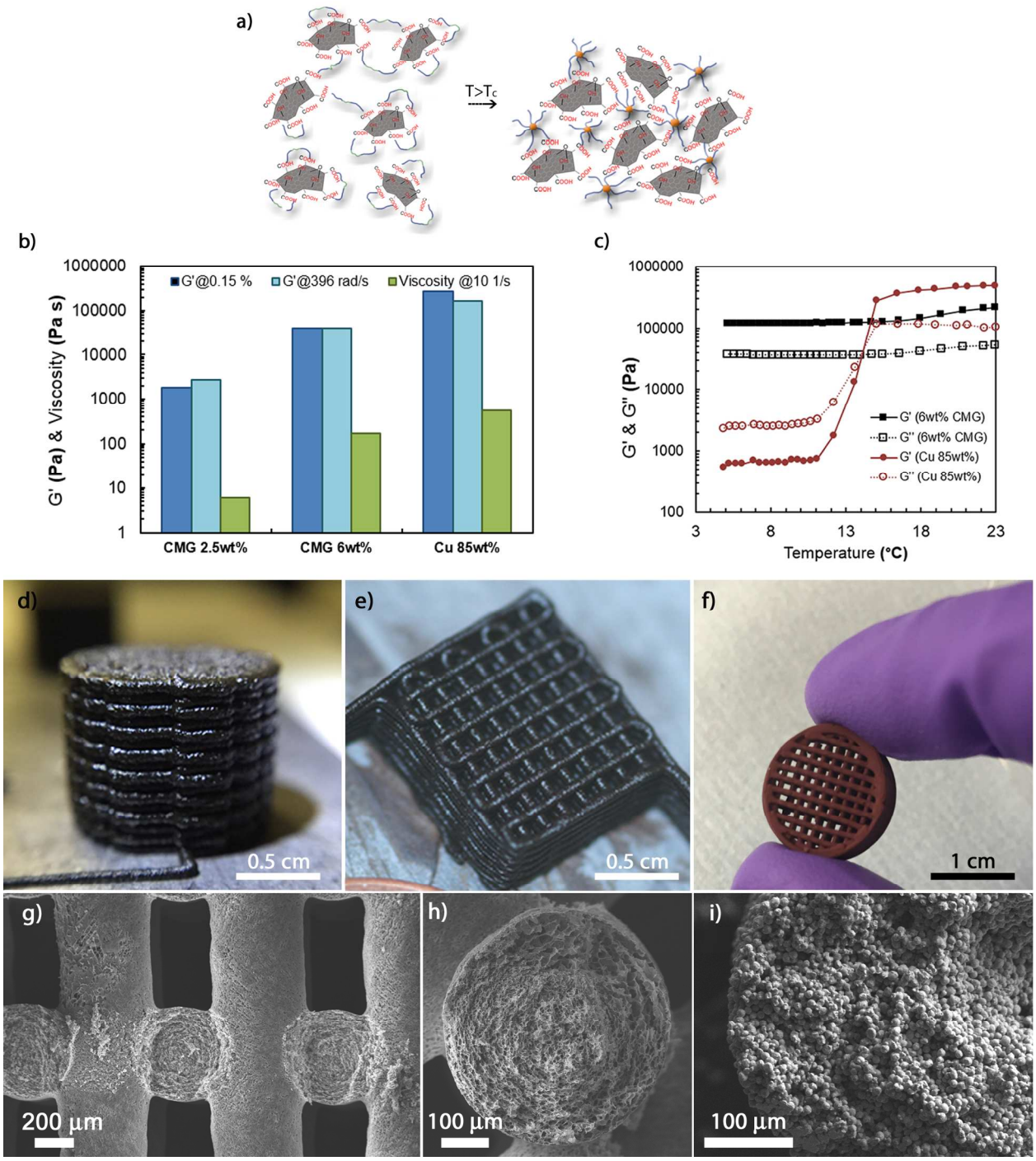

Figure 1. (a) Schematic illustration of CMG assembly with a thermo-responsive non-ionic triblock copolymer (CMG:F127 is 1:1). (b) Comparison of viscosity values and magnitude of the storage modulus (G' values obtained from two fingerprints: amplitude and frequency sweeps) for CMG (6 wt%) and Cu (85 wt%) water-based F127 inks. (c) Effect of temperature on viscoelasticity (temperature sweep) for CMG (6 wt%) and Cu (85 wt%) water-based F127 inks. (d-f) Images showing CMG and Cu 3D printed structures: (d) CMG cylinder (Ø~10 mm) made

to characterise rCMG bulk properties (i.e. conductivity and mechanical behaviour); (e) CMG grid designed for electrochemical testing; (f) Cu grid. (g-i) Images showing the internal microstructures after thermal reduction. (g) Cross section of a woodpile CMG aerogel showing that the filaments are stiff enough to preserve their shape across gaps. (h, i) internal microstructure of the CMG (h) and Cu (i) filaments.

The inks are shear thinning with viscosity and storage modulus (G') that increase with CMG concentration (Figure 1b). They flow smoothly under shear and rapidly recover their initial stiffness as the shear decreases. These inks can be printed on demand in the shape of cylinders (Figure 1d) for electrical and mechanical testing or grids (Figure 1f) for electrochemical and surface area characterization and also as an integrated device (Figure 2). Inks with lower concentrations (2.5 wt%) can be printed through the narrowest nozzles (100 μm) but the extruded filaments are not stiff enough (G' ~2kPa) to avoid deflection across spans. The storage modulus of inks with a CMG concentration of 6 wt% can reach values up to 100 kPa (Figure 1b, c). The filaments extruded from these inks are strong enough to support their weight without deflection across spans up to 0.6 mm (Figure 1g). Once printed, they maintain their shape whilst supporting subsequent layers (Figure 1d, e). F127 has an important role stabilising the flakes within the ink, avoiding restacking and agglomeration[32,33] while creating a homogeneous non-covalent network. These bonds can break down easily (providing shear thinning flow) and quickly rebuild, facilitating the recovery of the initial viscosity and elastic response once deposited. XPS spectra of as-printed CMG-F127 cylinders before thermal reduction confirm the ink formulation chemistry, displaying an increase of intensity for the peaks corresponding to F127 functional groups (Figure S2, Supporting Information).

Copper inks (Cu content 85 wt%) were prepared following the same process. These metallic conductive inks are also shear thinning and display a strong elastic behavior at temperatures above LCST (Figure 1b, c); their viscosity and storage modulus values are higher than those for

CMG inks (Figure 1b). These differences are due to the intrinsic characteristics of CMG flakes and Cu particles forming the networks (size, shape, surface area and density). Monitoring the viscoelastic properties during a temperature ramp provides a comparison of the two inks (Figure 1c). Both have lower G' and G'' values when the temperature drops below the LCST and the F127 hydrogel network breaks down; but with different behaviors and structures. The Cu ink behaves as a viscoelastic solid but the temperature drop breaks the network down completely, leading to a liquid-like system (G''>G', Figure 1e). For the CMG ink, G' and G'' only drop slightly and the elastic component still dominates (G'>G''); this ink behaves like a gel. This can be explained by the arrangement of 2D CMG flakes with high aspect ratio in a liquid crystal [34,22,35] and the small contribution of low amounts of F127 (only 6 wt%) to the overall stiffness.

At room temperature (> 20 °C) both inks have optimal viscoelastic flow for the 3D printing process (Figure 1c). We have printed a multicomponent electrode using two printing nozzles per layer (Figure 2a and video in the Supporting Information). The multicomponent design consists of two electrodes, the external walls contain the current collector and the inner walls are made of active material precursor (Figures 2a-d). Using the same F127 formulation facilitates bonding between the lines while avoiding additional binding agents. After printing, the electrodes are fast-frozen with liquid nitrogen, freeze-dried (Figure 2c) and thermally reduced (Figure 2d). The combination of printing and freezing templates the inner architecture of the CMG filaments. Extrusion through nozzles with long tips aligns the CMG flakes along parallel flow streamlines creating a radial arrangement[36] in the cross section (Figure 1h and 2g); while freezing avoids collapse, shrinkage and restacking of the flakes preserving a highly interconnected structure. FEGSEM images of the internal microstructure within the rCMG filaments evidence high macro-

porosity (~5-10 μm) with a concentric orientation of the pores along the radial direction (Figures 1g, h and 2g). This arrangement has also been observed in ceramics inks[36] and composites.[37,38]

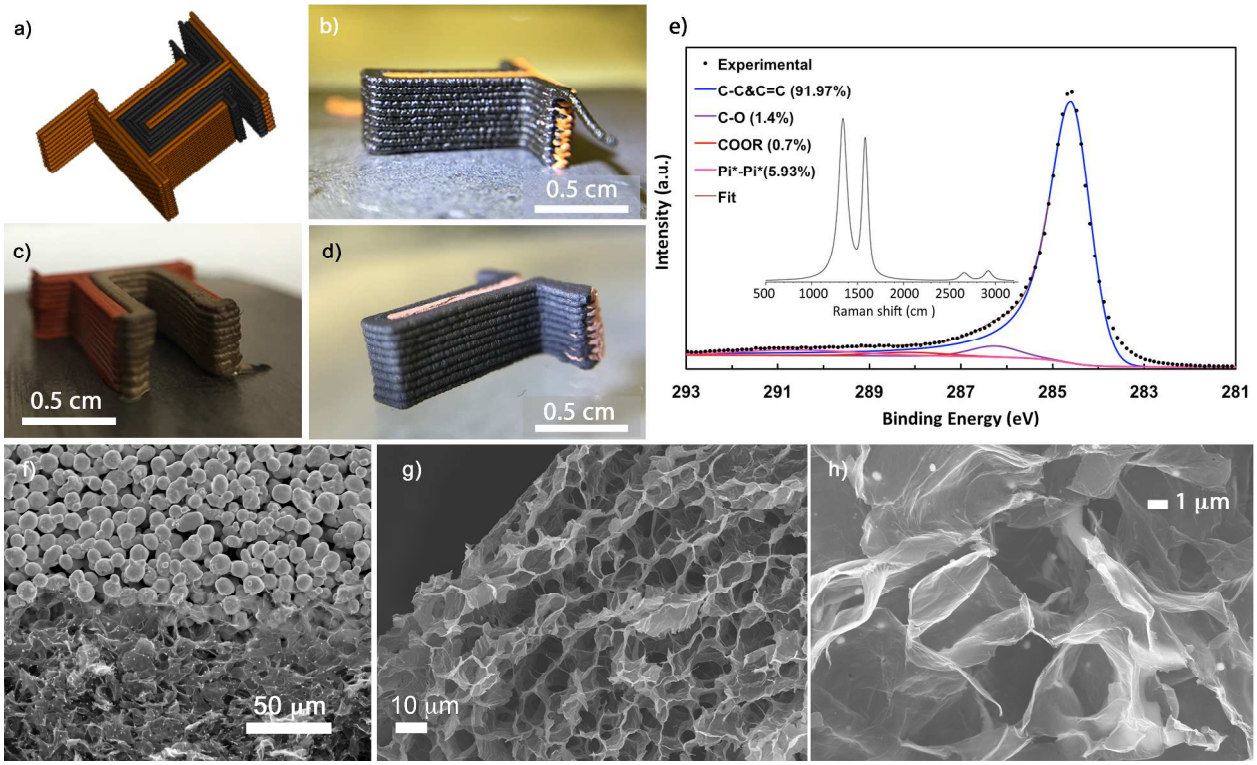

Figure 2. 3D printed graphene-based electrodes. (a) 3D model for the printing process. The external walls of the electrode containing the current collector (two adjacent Cu line) while the internal walls are made of the active material (two adjacent CMG lines). (b) Image of as printed CMG/Cu 1 leg component showing the fine details of the piled up filaments extruded through 500 μm nozzle using 6 wt% rCMG and 85 wt% Cu inks. (c) 2 legs electrode after freeze drying and (d) 1 leg component after simultaneous reduction (rCMG) and sintering (Cu) at 900°C (same component as b). (e) XPS and Raman spectrum show the effective sp^2 recovery, after thermal treatment. FESEM images. (f) SEM images at the rCMG/Cu interface (g) and inside the rCMG filaments (h). At the Cu/rCMG interface, the flakes fully cover the surface of the Cu particles showing very good physical contact. Cu nano-spheres formed on the graphene flakes surface were spotted throughout the active material, probably due to Cu evaporation and condensation. Copper does not wet carbon surfaces[39] so it is not surprising that vapour condenses to form spherical nanoparticles during thermal reduction.

Post-processing and charaterisation

Thermal reduction of CMGs and sintering of copper particles take place simultaneously. Cu particle size, shape and solid loading are adjusted to match the shrinkage (~ 5 % in volume) of the two materials during the thermal treatment. After reduction at 900 °C, we obtain a binder-free 3D structure consisting of a reduced graphene oxide aerogel (rCMG) in direct contact with sintered copper (Figure 2d). Using the same formulation base and optimizing conditions to avoid miss-matching shrinkage provided excellent contact between both materials (Figure 2f). The graphene oxide flakes cover the surface of the Cu particles, resulting in an interlocking interface between them. In fact the presence of some sub-microparticles (< 400 nm) of copper in the rCMG can also be observed due to the diffusion of copper into the rCMG (Figure 2f and 2h). XPS and Raman prove the quality of the partially reduced CMG prepared with F127 and confirm that the thermal reduction is effective (Figure 2e). The C/O ratio increases from 2 to 30, the spectrum displays sharper D and G peaks and, more importantly, the appearance of a 305 cm^{-1} width 2D peak at 2653 cm^{-1} which is characteristic of rGO (Figure 2e and S3c, Supporting Information). The reduction of 3D printed CMG cylinders leads to aerogels with a bulk density of ~30 mg cm^{-3}, a BET surface area of 193 ± 2 $m^2 g^{-1}$ (Figure S4) and electrical conductivity values of 90 ± 20 S m^{-1}. These values are comparable to those measured for other CMG derived aerogels and printed structures.[17,40] The interconnected porous architecture at the micro-scale favours the flow of the electrolyte across the 3D network of active material thus facilitating ion transport. BET and TEM (Figure S5, Supporting Information) confirm the presence of mesopores (2-50 nm) that are considered beneficial for supercapacitor devices.[41]

Cyclic compression tests were coupled with electrical conductivity measurements on 3D printed rCMG cylinders; they show elastic-brittle behaviour with similar strengths to other aerogels with similar densities.[42] During compression they initially exhibit reversible elastic behaviour (up to

10% strain) with consistent conductivity values after the second cycle (Figure S6, Supporting Information). Increasing the compression strain above 10% results in a change of the stress-strain slope due to 'yielding' and microcracking at 18-20% that leads to a slight drop in conductivity values.

Electrochemical characterisation

Cyclic Voltammetry (CV) of the 3 electrodes system using imidazolium-based ionic liquid (EMI-TFSI) - selected as electrolyte because of the wide electrochemical stability window of ionic liquids (ILs) (energy density is directly proportional to the square voltage) [43] - is stable up to 3V (Figure S8). The specific capacitance of the rCMG self-supporting electrodes calculated from the CVs is 16 F g^{-1} at 2 mV s^{-1} (Supporting Information). Additionally, the symmetric configuration - using two coupled multi-material printed electrodes mounted as a symmetrical supercapacitor (Figure 3) - demonstrates the potential of this approach to manufacture bespoke energy storage devices (Figure 3, 4, 5 and 6).

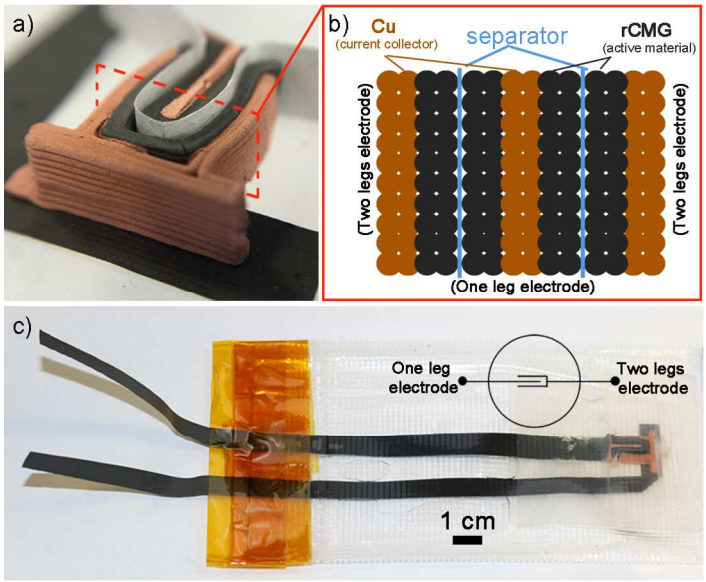

Figure 3. (a) Image of mounted supercapacitor device components prior testing; including cellulose paper separator, positive and negative electrodes. (b) Scheme of the cross section showing a model of the Cu and rCMG filaments and separator. (c) Mounted device ready for testing: image of the vacuum-sealed supercapacitor pouch cell with protruding Al foil tabs; the inset shows a simplified diagram of the system.

Impedance spectroscopy (EIS) has been previously used to analyze the performance of devices, for example to differentiate between the resistance and the capacitance of a supercapacitor.[44-46] The key-plot of EIS measurements is the Nyquist plot, which represents the imaginary part of the impedance ($-Z_{im}$) versus the real part (Z_{real}). Z_{real} is related to the resistance of the electrolyte, the electrode, the contacts and any other faradaic resistance; Z_{im} is related to the charge storage mechanism and the reaction controlled by diffusion of the electrolyte.[47] From the generated Nyquist plots it is possible to deduce many features related to the resistance (illustrated in Figure 4a).[45-46] The schematic representation has three different regions: i) semi-circle (high frequencies), ii) 45º line (medium frequencies) and iii) vertical line (low frequencies) (Figure 4a).

i) The bulk electrolyte resistance, $R_{s,}$ (the current collector could also be included[48]) can be identified at high frequencies (> 1 kHz) from the generated Nyquist plots (Figure 4). The electrolyte and electrode composition were the same for both configurations, but R_s is 5 times higher for the 3-electrode system than for the symmetric one (64 Ω and 13 Ω respectively) due to the smaller resistance of its current collector. The semi-circle loop is also observed at high frequencies (defined as a RC-circuit (R_i-C_i)) for the 3-electrodes system (Figure 4b).[45] This is related to the double layer capacitance and charge-transfer resistance[48] (Figure 4a). C_i represents the interfacial capacitance at the interface and α_i ($0<\alpha_i<1$) illustrates the non-ideal behaviour of C_i. When R_i tends to infinite the interface is blocked and the cell works like a dielectric capacitor; when it tends to cero the RC-loop disappears and the Nyquist plot has the same shape that the ideal supercapacitor (Figure 4a). Generally, R_i decreases if the electrolyte conductivity is increased or the resistivity of the interface current collector-carbon electrode decreased.[45-46] For the symmetric system, the Nyquist plot does not display the semi-circle loop (Figure 4b) and R_i

tends to a very low value. The same electrolyte is used in both configurations but the total impedance for the multi-material printed device (symmetric system) is significantly lower, demonstrating the good contact between the rCMG electrode and the copper current collector (Figure 2f). These results prove that printing both components (electrode and current collector) together favours the electronic contact between them.

ii) The middle frequency region (45º line, Figure 4a) is due to the resistance depending on the frequency (R_W); R_w is associated with the electrolyte diffusion and penetration in the pores of the electrode.[46,49] For both systems, R_w is very small (Figure 4b) due to the large pores within the rCMG aerogel (Figure 2g).

iii) At low frequency values (<1 kHz) the cell behaviour is represented by the circuit $R_{sc}(w)$-C(w) (Figure 4a). Where C(w) is the cell capacitance and $R_{sc}(w)$ the series resistance of the cell ($R_{sc}(w) = R_s + R_i + R_W$). $R_{sc}(w)$ depends on the impedance contact and both of them vary with frequency. An ideal supercapacitor presents a vertical tail (Figure 4a); a non-vertical slope indicates that other processes (besides double layer formation) such as diffusion limitations or faradaic reactions[48-49] might be taking place. In the Nyquist plots for both configurations, the tails are slightly tilted (Figure 4b) likely due to the high viscosity of the IL at room temperature.

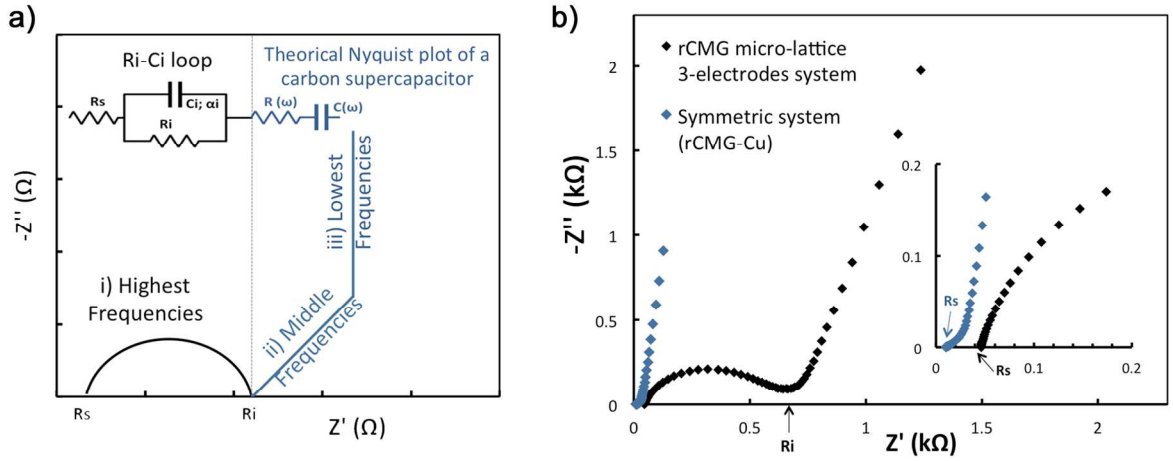

Figure 4. a) Typical Nyquist plot of a carbon-carbon supercapacitor. It includes high to low frequency behaviour of a supercapacitor with the equivalent circuits (Rs is the high frequency resistance, Ri the resistance of the active material/current collector interface, Ci the interface capacitance with the dispersion parameter αi, R(ω) a part of the supercapacitor resistance depending on the frequency and C(ω) the supercapacitor cell capacitance) and b) Nyquist plots recorded from 100 kHz to 10 mHz, for the 3-electrodes (blue) and symmetric (black) systems in EMI-TFSI electrolyte, with their corresponding magnification of high and mid frequencies response.

From the EIS results it is also possible to calculate the total effective capacitance of the cell and the relaxation time (τ, or time required to discharge the half of the energy stored in the device) using Equations 1 and 2, respectively:[46]

$$C(\omega) = C_{real}(\omega) - jC_{im}(\omega) = \frac{-Z_{im}(\omega)}{\omega|Z(\omega)|^2} - j\frac{Z_{real}(\omega)}{\omega|Z(\omega)|^2} \quad \text{[Eq. 1]}$$

$$\tau_0 = \frac{1}{f_0} = \frac{2\pi}{\omega} \quad \text{[Eq. 2]}$$

Where j is the imaginary number, C_{real} the real part component of C and C_{im} the imaginary, f_0 is the frequency reached at the maximum of C_{im} and ω is the angular frequency.[47] The imaginary and real parts of the capacitance are plotted versus frequency (Figure 5).

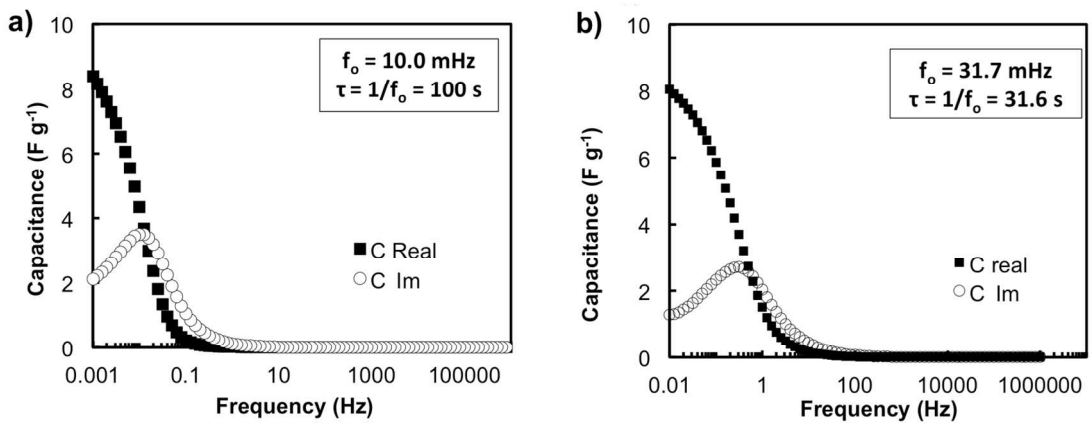

Figure 5. Imaginary (C_{im}) and real (C_{real}) parts of the capacitance plotted versus frequency (logarithmic scale) calculated from EIS results for the (a) 3-electrodes and (b) symmetric system, in EMI-TFSI electrolyte at 0V, and their relaxation times (τ), which correspond to the inverse of the frequency at the maximum of C_{im} curves (f_0)

The relaxation time is related to the ion diffusion, so the expected values for an IL are larger than those for aqueous electrolytes (< 10s), the value for the symmetric system is 31.6s, 3 times smaller than the obtained for the 3-electrode system due to the good electronic properties of the printed device.

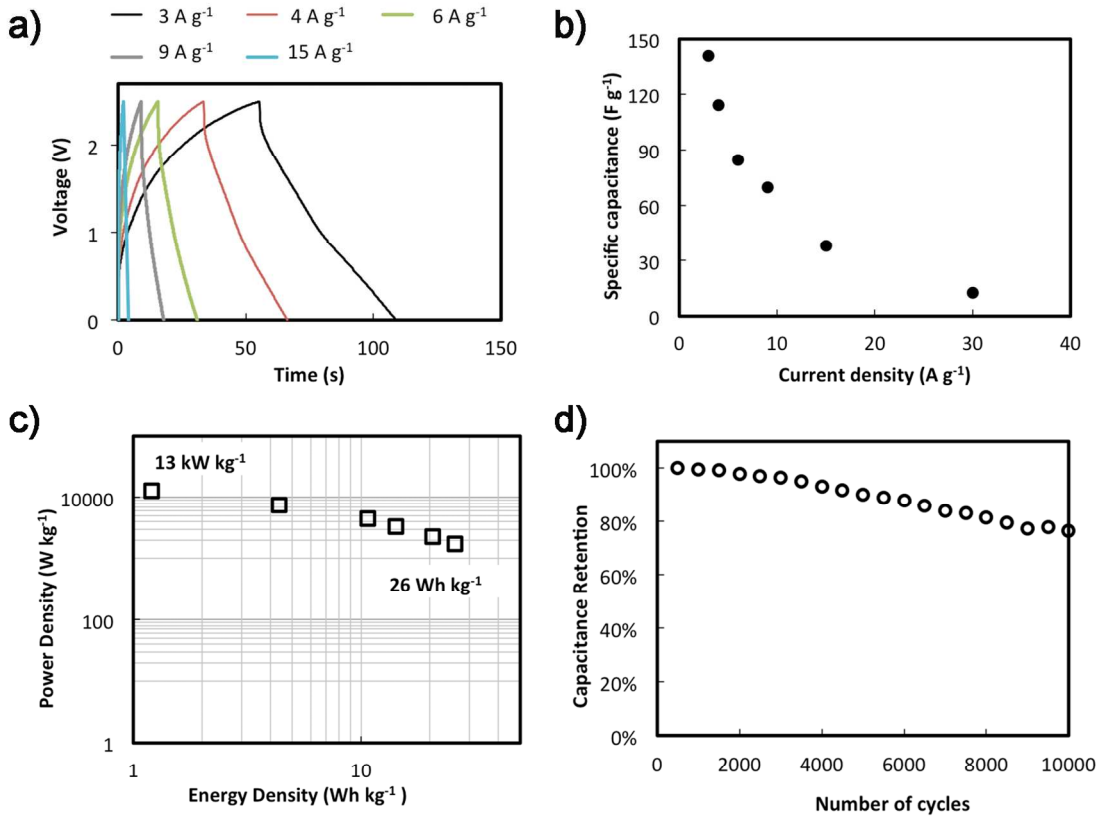

Figure 6. a) Galvanostatic charge−discharge curves at increasing current densities for the symmetric device; **b)** specific capacitance versus current density calculated from galvanostatic charge-discharge curves; **c)** Ragone plot calculated from galvanostatic charge−discharge curves registered considering only the mass of the two electrodes of the supercapacitor device; and **d)** cycle performance at 15 A g^{-1} for 10000 cycles.

The capacitance value calculated at low frequency (close to the vertical line of the Nyquist Plot) is around 8 F g^{-1} (Figure 5). This is the expected value for a rCMG aerogel with a BET of 193 ± 2 m^2 g^{-1}, also in agreement with the results obtained by CVs (16 F g^{-1} at 2 mV s^{-1}, Figure S8) and with the galvanostatic charge-discharge curves (13 F g^{-1}) registered at high current density (30 A g^{-1}) for the symmetric system (Figure 6a-b). At lower current densities (3A g^{-1}) the calculated capacitance increases up to 140 F g^{-1} which could be attributed to redox reactions of the rCMG's residual oxygen functional groups (Figure 2e). As a result the specific energy and power

densities reach values of 26 Wh kg^{-1} (at the power density of 1.7 kW kg^{-1}) and 13 kW kg^{-1} (at the energy density of 1.2 Wh kg^{-1}), respectively (figure 6c). The capacitance retention at 15 A g^{-1} rated 80% after 10,000 cycles (Figure 6d), indicating that the multi-material printed device has a promising viability and long term stability. Optimization of the design and/or materials to improve the performance of the final device compared vs. other manufacturing approaches is beyond the scope of this proof of concept. Our results open up multiple possibilities, for example in developing components for other energy devices as anodes for Lithium ion batteries; and the processing of carbon materials doped with nanoparticles or activated graphene (using chemical, hydrothermal or physical activation) to enhance their initial surface area and improve the capacitance (pseudocapacitance) of the final devices.

CONCLUSIONS

The formulation of thermo-responsive inks using F127 provides a robust, flexible and easily scalable-up approach to design and fabricate multicomponent graphene-based electrodes and devices for EES. They can be designed to provide enhanced mechanical performance, effective packing of rCMG, low active material density, enhanced interface contact and electrical properties.

This proof of concept demonstrates the capabilities of additive manufacturing techniques to make electrodes and devices for EES applications in bespoke configurations, which will eventually allow tailored designs that could be integrated in confined spaces. The thermo-responsive water-based hydrogel inks can be adapted to a broad range of materials from graphene to metals and ceramics, opening up new possibilities across disciplines, from EES devices to health and engineering; allowing the fabrication of customised devices tailored to fit

applications with complex geometries. The formulations and strategy developed in this work will contribute to advance in the field of EES, in particular on the fabrication of multimaterials supercapacitors, battery electrodes and devices rationally designed to improve the interface between the materials and to optimize performance by decreasing the resistance of printed devices.

ASSOCIATED CONTENT

Supporting Information: Extended methods for electrochemical characterization; BET characterization (PDF); and CuCMG electrode 3D printing (.avi).

ABBREVIATIONS

PEO, Poly(ethylene oxide);PPO, poly(propylene oxide).

AUTHOR INFORMATION

Corresponding Authors

*E-mail: GarciaRochaV@cardiff.ac.uk

*E-mail: Esther.GTunon@liverpool.ac.uk

ORCID

Victoria G. Rocha: 0000-0001-6125-8556

Esther García-Tuñón: 0000-0001-9507-4501

The authors declare no competing financial interest

Author Contributions

The manuscript was written through contributions of all authors. All authors have given approval to the final version of the manuscript.

ACKNOWLEDGEMENTS

VGR would like to thank the European Commission (FP7—Marie Curie Intra European Fellowship GRAPES). EGT, ES and MS would like to acknowledge the EPSRC Grant graphene 3D networks (EP/K01658X/1). EF would like to acknowledge the CASC (Centre for Advanced Structural Ceramics). NN acknowledged the Junior Research Fellowship, Imperial College London. CB would like to thank the Spanish Government the Jose Castillejo Mobility grant (CAS15/00329) and the EU (Graphene Flagship Core 1).

REFERENCES

(1) Akbari, A.; Sheath, P.; Martin, S. T.; Shinde, D. B.; Shaibani, M.; Banerjee, P. C.; Tkacz, R.; Bhattacharyya, D.; Majumder, M. Large-Area Graphene-Based Nanofiltration Membranes by Shear Alignment of Discotic Nematic Liquid Crystals of Graphene Oxide. *Nat Commun* **2016**, DOI:10.1038/ncomms10891.
(2) Singh, V.; Joung, D.; Zhai, L.; Das, S.; Khondaker, S. I.; Seal, S. Graphene Based Materials: Past, Present and Future. *Prog. Mater. Sci.* **2011,** *56* (8), 1178-1271.
(3) Yao, Y. G.; Fu, K. K.; Yan, C. Y.; Dai, J. Q.; Chen, Y. N.; Wang, Y. B.; Zhang, B. L.; Hitz, E.; Hu, L. B. Three-Dimensional Printable High-Temperature and High-Rate Heaters. *ACS Nano* **2016,** *10* (5), 5272-5279.
(4) Gu, W. T.; Yushin, G. Review of Nanostructured Carbon Materials for Electrochemical Capacitor Applications: Advantages and Limitations of Activated Carbon, Carbide-Derived Carbon, Zeolite-Templated Carbon, Carbon Aerogels, Carbon Nanotubes, Onion-Like Carbon, and Graphene. *Wiley Interdiscip. Rev.: Energy Environ.* **2014,** *3* (5), 424-473.
(5) Botas, C.; Carriazo, D.; Zhang, W.; Rojo, T.; Singh, G. Silicon-Reduced Graphene Oxide Self-Standing Composites Suitable as Binder-Free Anodes for Lithium-Ion Batteries. *ACS Appl. Mater. Interfaces* **2016,** *8* (42), 28800-28808.
(6) Gonzalez, Z.; Botas, C.; Blanco, C.; Santamaria, R.; Granda, M.; Alvarez, P.; Menendez, R. Thermally Reduced Graphite and Graphene Oxides in Vrfbs. *Nano Energy* **2013,** *2* (6), 1322-1328.
(7) Quesnel, E.; Roux, F.; Emieux, F.; Faucherand, P.; Kymakis, E.; Volonakis, G.; Giustino, F.; Martin-Garcia, B.; Moreels, I.; Gursel, S. A.; Yurtcan, A. B.; Di Noto, V.; Talyzin, A.; Baburin,

I.; Tranca, D.; Seifert, G.; Crema, L.; Speranza, G.; Tozzini, V.; Bondavalli, P.; Pognon, G.; Botas, C.; Carriazo, D.; Singh, G.; Rojo, T.; Kim, G.; Yu, W. J.; Grey, C. P.; Pellegrini, V. Graphene-Based Technologies for Energy Applications, Challenges and Perspectives. *2D Mater.* **2015,** *2* (3).
(8) Fu, K.; Yao, Y. G.; Dai, J. Q.; Hu, L. B. Progress in 3d Printing of Carbon Materials for Energy-Related Applications. *Adv. Mater.* **2017,** *29* (9).
(9) Ambrosi, A.; Pumera, M. 3d-Printing Technologies for Electrochemical Applications. *Chem. Soc. Rev.* **2016,** *45* (10), 2740-2755.
(10) Zhu, C.; Liu, T.; Qian, F.; Chen, W.; Chandrasekaran, S.; Yao, B.; Song, Y.; Duoss, E. B.; Kuntz, J. D.; Spadaccini, C. M.; Worsley, M. A.; Li, Y. 3d Printed Functional Nanomaterials for Electrochemical Energy Storage. *Nano Today* **2017**, DOI:10.1016/j.nantod.2017.06.007.
(11) Wei, M.; Zhang, F.; Wang, W.; Alexandridis, P.; Zhou, C.; Wu, G. 3d Direct Writing Fabrication of Electrodes for Electrochemical Storage Devices. *J Power Sources* **2017,** *354*, 134-147.
(12) Tian, X.; Jin, J.; Yuan, S.; Chua, C. K.; Tor, S. B.; Zhou, K. Emerging 3d-Printed Electrochemical Energy Storage Devices: A Critical Review. *Adv Energy Mater* **2017,** *7* (17), 1700127-n/a.
(13) Zhang, F.; Wei, M.; Viswanathan, V. V.; Swart, B.; Shao, Y.; Wu, G.; Zhou, C. 3d Printing Technologies for Electrochemical Energy Storage. *Nano Energy* **2017**, DOI:http://dx.doi.org/10.1016/j.nanoen.2017.08.037.
(14) Vlad, A.; Singh, N.; Galande, C.; Ajayan, P. M. Design Considerations for Unconventional Electrochemical Energy Storage Architectures. *Adv Energy Mater* **2015,** *5* (19), 1402115.
(15) Markoulidis, F.; Lei, C.; Lekakou, C.; Duff, D.; Khalil, S.; Martorana, B.; Cannavaro, I. A Method to Increase the Energy Density of Supercapacitor Cells by the Addition of Multiwall Carbon Nanotubes into Activated Carbon Electrodes. *Carbon* **2014,** *68*, 58-66.
(16) Zhu, C.; Han, T. Y. J.; Duoss, E. B.; Golobic, A. M.; Kuntz, J. D.; Spadaccini, C. M.; Worsley, M. A. Highly Compressible 3d Periodic Graphene Aerogel Microlattices. *Nat Commun* **2015,** *6*.
(17) García-Tuñon, E.; Barg, S.; Franco, J.; Bell, R.; Eslava, S.; D'Elia, E.; Maher, R. C.; Guitian, F.; Saiz, E. Printing in Three Dimensions with Graphene. *Adv. Mater.* **2015,** *27* (10), 1688-1693.
(18) Jakus, A. E.; Secor, E. B.; Rutz, A. L.; Jordan, S. W.; Hersam, M. C.; Shah, R. N. Three-Dimensional Printing of High-Content Graphene Scaffolds for Electronic and Biomedical Applications. *ACS Nano* **2015,** *9* (4), 4636-4648.
(19) De Marco, M.; Markoulidis, F.; Menzel, R.; Bawaked, S. M.; Mokhtar, M.; Al-Thabaiti, S. A.; Basahel, S. N.; Shaffer, M. S. P. Cross-Linked Single-Walled Carbon Nanotube Aerogel Electrodes Via Reductive Coupling Chemistry. *J Mater Chem A* **2016,** *4* (15), 5385-5389.
(20) Worsley, M. A.; Merrill, M. D.; Charnvanichborikarn, S.; Kucheyev, S. O.; Satcher Jr, J. H.; Stadermann, M.; Biener, J.; Baumann, T. F. Thick, Binder-Free Carbon-Nanotube-Based Electrodes for High Power Applications. *ECS J. Solid State Sci. Technol.* **2013,** *2* (10), M3140-M3144.
(21) Worsley, M. A.; Pham, T. T.; Yan, A. M.; Shin, S. J.; Lee, J. R. I.; Bagge-Hansen, M.; Mickelson, W.; Zettl, A. Synthesis and Characterization of Highly Crystalline Graphene Aerogels. *ACS Nano* **2014,** *8* (10), 11013-11022.

(22) Yao, B. W.; Chen, J.; Huang, L.; Zhou, Q. Q.; Shi, G. Q. Base-Induced Liquid Crystals of Graphene Oxide for Preparing Elastic Graphene Foams with Long-Range Ordered Microstructures. *Adv. Mater.* **2016,** *28* (8), 1623-1629.
(23) Li, W.; Li, Y.; Su, M.; An, B.; Liu, J.; Su, D.; Li, L.; Li, F.; Song, Y. Printing Assembly and Structural Regulation of Graphene Towards Three-Dimensional Flexible Micro-Supercapacitors. *J Mater Chem A* **2017,** *5* (31), 16281-16288.
(24) Zhu, C.; Liu, T.; Qian, F.; Han, T. Y.-J.; Duoss, E. B.; Kuntz, J. D.; Spadaccini, C. M.; Worsley, M. A.; Li, Y. Supercapacitors Based on Three-Dimensional Hierarchical Graphene Aerogels with Periodic Macropores. *Nano Letters* **2016,** *16* (6), 3448-3456.
(25) Smay, J. E.; Gratson, G. M.; Shepherd, R. F.; Cesarano, J.; Lewis, J. A. Directed Colloidal Assembly of 3d Periodic Structures. *Adv. Mater.* **2002,** *14* (18), 1279-+.
(26) Sun, K.; Wei, T. S.; Ahn, B. Y.; Seo, J. Y.; Dillon, S. J.; Lewis, J. A. 3d Printing of Interdigitated Li-Ion Microbattery Architectures. *Adv. Mater.* **2013,** *25* (33), 4539-4543.
(27) Fu, K.; Wang, Y. B.; Yan, C. Y.; Yao, Y. G.; Chen, Y. A.; Dai, J. Q.; Lacey, S.; Wang, Y. B.; Wan, J. Y.; Li, T.; Wang, Z. Y.; Xu, Y.; Hu, L. B. Graphene Oxide-Based Electrode Inks for 3d-Printed Lithium-Ion Batteries. *Adv. Mater.* **2016,** *28* (13), 2587-2594.
(28) Marcano, D. C.; Kosynkin, D. V.; Berlin, J. M.; Sinitskii, A.; Sun, Z. Z.; Slesarev, A.; Alemany, L. B.; Lu, W.; Tour, J. M. Improved Synthesis of Graphene Oxide. *ACS Nano* **2010,** *4* (8), 4806-4814.
(29) Feilden, E.; Blanca, E. G. T.; Giuliani, F.; Saiz, E.; Vandeperre, L. Robocasting of Structural Ceramic Parts with Hydrogel Inks. *J. Eur. Ceram. Soc.* **2016,** *36* (10), 2525-2533.
(30) Franco, J.; Hunger, P.; Launey, M. E.; Tomsia, A. P.; Saiz, E. Direct Write Assembly of Calcium Phosphate Scaffolds Using a Water-Based Hydrogel. *Acta Biomater.* **2010,** *6* (1), 218-228.
(31) Vasita, R.; Mani, G.; Agrawal, C. M.; Katti, D. S. Surface Hydrophilization of Electrospun Plga Micro-/Nano-Fibers by Blending with Pluronic® F-108. *Polymer* **2010,** *51* (16), 3706-3714.
(32) Zu, S. Z.; Han, B. H. Aqueous Dispersion of Graphene Sheets Stabilized by Pluronic Copolymers: Formation of Supramolecular Hydrogel. *J Phys Chem C* **2009,** *113* (31), 13651-13657.
(33) Hong, B. J.; Compton, O. C.; An, Z.; Eryazici, I.; Nguyen, S. T. Successful Stabilization of Graphene Oxide in Electrolyte Solutions: Enhancement of Biofunctionalization and Cellular Uptake. *ACS Nano* **2012,** *6* (1), 63-73.
(34) Akbari, A.; Sheath, P.; Martin, S. T.; Shinde, D. B.; Shaibani, M.; Banerjee, P. C.; Tkacz, R.; Bhattacharyya, D.; Majumder, M. Large-Area Graphene-Based Nanofiltration Membranes by Shear Alignment of Discotic Nematic Liquid Crystals of Graphene Oxide. *Nat Commun* **2016,** *7*.
(35) Kim, J. E.; Han, T. H.; Lee, S. H.; Kim, J. Y.; Ahn, C. W.; Yun, J. M.; Kim, S. O. Graphene Oxide Liquid Crystals. *Angew Chem Int Edit* **2011,** *50* (13), 3043-3047.
(36) Román-Manso, B.; Figueiredo, F. M.; Achiaga, B.; Barea, R.; Pérez-Coll, D.; Morelos-Gómez, A.; Terrones, M.; Osendi, M. I.; Belmonte, M.; Miranzo, P. Electrically Functional 3d-Architectured Graphene/Sic Composites. *Carbon* **2016,** *100*, 318-328.
(37) Román-Manso, B.; Chevillotte, Y.; Osendi, M. I.; Belmonte, M.; Miranzo, P. Thermal Conductivity of Silicon Carbide Composites with Highly Oriented Graphene Nanoplatelets. *J. Eur. Ceram. Soc.* **2016,** *36* (16), 3987-3993.
(38) Centeno, A.; Rocha, V. G.; Alonso, B.; Fernandez, A.; Gutierrez-Gonzalez, C. F.; Torrecillas, R.; Zurutuza, A. Graphene for Tough and Electroconductive Alumina Ceramics. *J. Eur. Ceram. Soc.* **2013,** *33* (15-16), 3201-3210.

(39) Dezellus, O.; Eustathopoulos, N. The Role of Van Der Waals Interactions on Wetting and Adhesion in Metal Carbon Systems. *Scripta Mater* **1999,** *40* (11), 1283-1288.
(40) Barg, S.; Perez, F. M.; Ni, N.; do Vale Pereira, P.; Maher, R. C.; Garcia-Tunon, E.; Eslava, S.; Agnoli, S.; Mattevi, C.; Saiz, E. Mesoscale Assembly of Chemically Modified Graphene into Complex Cellular Networks. *Nat Commun* **2014,** *5*, 4328.
(41) Simon, P.; Gogotsi, Y. Materials for Electrochemical Capacitors. *Nat Mater* **2008,** *7* (11), 845-854.
(42) Ni, N.; Barg, S.; Garcia-Tunon, E.; Macul Perez, F.; Miranda, M.; Lu, C.; Mattevi, C.; Saiz, E. Understanding Mechanical Response of Elastomeric Graphene Networks. *Scientific Reports* **2015,** *5*, 13712.
(43) Peng, C. X.; Yang, L.; Fang, S. H.; Wang, J. X.; Zhang, Z. X.; Tachibana, K.; Yang, Y.; Zhao, S. Y. Electrochemical Behavior of Copper Current Collector in Imidazolium-Based Ionic Liquid Electrolytes. *J Appl Electrochem* **2010,** *40* (3), 653-662.
(44) Nian, Y. R.; Teng, H. S. Influence of Surface Oxides on the Impedance Behavior of Carbonbased Electrochemical Capacitors. *J Electroanal Chem* **2003,** *540*, 119-127.
(45) Portet, C.; Taberna, P. L.; Simon, P.; Laberty-Robert, C. Modification of Al Current Collector Surface by Sol-Gel Deposit for Carbon-Carbon Supercapacitor Applications. *Electrochim Acta* **2004,** *49* (6), 905-912.
(46) Lewandowski, A.; Olejniczak, A.; Galinski, M.; Stepniak, I. Performance of Carbon-Carbon Supercapacitors Based on Organic, Aqueous and Ionic Liquid Electrolytes. *J Power Sources* **2010,** *195* (17), 5814-5819.
(47) Yao, F.; Pham, D. T.; Lee, Y. H. Carbon-Based Materials for Lithium-Ion Batteries, Electrochemical Capacitors, and Their Hybrid Devices. *Chemsuschem* **2015,** *8* (14), 2284-2311.
(48) Béguin, F.; Frackowiak, E. *Supercapacitors: Materials, Systems, and Applications*, 2013, DOI:10.1002/9783527646661.
(49) Nian, Y.-R.; Teng, H. Influence of Surface Oxides on the Impedance Behavior of Carbon-Based Electrochemical Capacitors. *J Electroanal Chem* **2003,** *540*, 119-127.

Table of Contents Graphic